

Article

Active Tectonics Revealed by River Profiles along the Puqu Fault

Ping Lu ¹ and Yu Shang ^{2,*}

¹ College of Surveying and Geo-Informatics, Tongji University, Siping Road 1239, Shanghai 200092, China; E-Mail: luping@tongji.edu.cn

² School of Environmental and Chemical Engineering, Shanghai University, Nanchen Road 333, Shanghai 200444, China

* Author to whom correspondence should be addressed; E-Mail: yushang@shu.edu.cn; Tel./Fax: +86-21-6613-7734.

Academic Editor: Jun Xu

Received: 12 January 2015 / Accepted: 6 April 2015 / Published: 17 April 2015

Abstract: The Puqu Fault is situated in Southern Tibet. It is influenced by the eastward extrusion of Northern Tibet and carries the clockwise rotation followed by the southward extrusion. Thus, the Puqu Fault is bounded by the principal dynamic zones and the tectonic evolution remains active alongside. This study intends to understand the tectonic activity in the Puqu Fault Region from the river profiles obtained from the remotely sensed satellite imagery. A medium resolution Digital Elevation Model (DEM, 20 m) was generated from an Advanced Spaceborne Thermal Emission and Reflection Radiometer (ASTER) stereo pair of images and the stream network in this region was extracted from this DEM. The indices of slope and drainage area were subsequently calculated from this ASTER DEM. Based on the stream power law, the area-slope plots of the streams were delineated to derive the indices of channel concavity and steepness, which are closely related to tectonic activity. The results show the active tectonics varying significantly along the Puqu Fault, although the potential influence of glaciations may exist. These results are expected to be useful for a better understanding of tectonic evolution in Southeastern Tibet.

Keywords: stream network; river profiles; channel equilibrium; tectonics; ASTER DEM; Puqu Fault; Southern Tibet

1. Introduction

Empirical observations have indicated that steep topography may be closely related to rapid uplift [1]. In particular, several studies have revealed that landscape surfaces are efficient indicators related to tectonic uplift and deformation processes [2–4]. In addition, some studies argued that hillslopes may be influenced by potential balance between erosion and soil production rates [1,5–7]. These tectonic activities may alter river network mainly through changes of fluvial incision rates and stream diversion by modifying erosion base level [8–10]. The river network, on the other hand, is continuously responding to tectonic forcing and accordingly provides potential meaningful information about spatial variation of uplift across landscape [1,11–14]. Furthermore, the drainage network may continuously adjust to changes of surface slope, and consequently it shows potential in recording information related to evolution of faults and folds [15,16].

Empirical observations from river systems across the earth in past decades also denoted a consistent power-law relationship between channel slope and drainage area. Theoretical arguments for both detachment-limited and transport-limited erosion regimes strongly suggested that rock uplift rate exerts first-order control on this relationship [17,18]:

$$S = k_s A^{-\theta} \quad (1)$$

S indicates local channel slope, A is upstream drainage area and k_s and θ are channel steepness and concavity indices, respectively. This power-law relationship has been widely used in past studies, and its usefulness has been verified in both detachment-limited and transport-limited river systems. For example, Snyder *et al.* [19] have analyzed landscape responses to tectonic forcing in the Mendocino Triple Junction region in Northern California; Lague *et al.* [20] have estimated uplift rate and erodibility using the area-slope relationship in Brittany, France; Kirby and Whipple [21] have successfully quantified differential rock uplift rates through the stream profile analysis in the area of Siwalik Hills in Central Nepal; Schoenbohm *et al.* [4] have calculated the surface uplift in the Red River region in Yunnan Province of China; Shahzad *et al.* [14] employed Shuttle Radar Topography Mission (SRTM) data to extract draining network for regional tectonic analysis in Potwar Plateau in Northern Pakistan; a similar approach was utilized by Shahzad *et al.* [22] to understand tectonic geomorphology in Kaghan Valley in Northern Pakistan; Anoop *et al.* [23] suggested the existence of large-scale tectonic deformation from the calculated geomorphic indices across the Kaurik-Chango Fault region in the Upper Spiti Valley, Northwestern Himalaya; Fuchs *et al.* [24] estimated the impacts of tectonics and climate change on the Panj River in Pamir Plateau through an analysis of fluvial incision and stream profile of the Panj river network. These studies have revealed a direct power-law relationship between the steepness index k_s and the rock uplift rate U .

Since the channel concavity θ and the steepness k_s indicate spatial variation of rock uplift rate, river profile parameters derived from regressions on logarithm slope-area data allow to extract information about regional tectonics. In particular, the analysis of these channel gradients is often on the basis of Digital Elevation Model (DEM) [25]. Several methods have been proposed to extract river profiles and channel parameters from DEM. For example, Snyder *et al.* [19] and Kirby and Whipple [21] have developed a group of built-in functions in ARC/INFO to create flow accumulation arrays and delineate drainage basins; Mahmood and Gloaguen [26] calculated the indices of relative active tectonics

(IRAT) in the Geography Information System (GIS) from a DEM in Hindu Kush region. In addition, scientific programming languages such as Matlab and SAS scripts were integrated in GIS to color-code stream profiles by their steepness and concavity indices: Shahzad *et al.* [22] have developed the package TecDEM using MATLAB for drainage network partition and river profile analysis from DEM and this package was also used by Vezzoli *et al.* [27] to extract the fluvial network in Western Greater Caucasus. Other widely-used packages able to extract river profiles from DEM include LANDLORD [28] and Terrain Analysis System (TAS, [29]). A recent study attempted to use LiDAR (Light Detection and Ranging) to generate a DEM for river profile extraction [30]; however, the cost of LiDAR is very high, which may decrease its practical use in the field.

This study intends to understand the tectonic activities in the Puqu Fault Region by using the power-law relationship between channel slope and drainage area. The topographic indices of river profile shape and character were derived from a freely available Advanced Spaceborne Thermal Emission and Reflection Radiometer (ASTER) DEM. Past studies have reported that in the boundary of the Southeastern Tibet Plateau, rivers are responding to tectonic uplift and deformation, recording temporal and spatial differences in rock uplift rates [4,31]. The river network in the Puqu Fault area, which is situated in the southeastern margin of the Tibet Plateau with numerous tributaries flowing into it, is expected to be a sensitive recorder of the spatial and temporal variations in active tectonics in the eastern Karakoram–Jiali Fault Zone (KJFZ). This study chiefly concentrates on extracting tectonics from topography by analyzing river elevation profiles for these tributaries flowing into the Puqu Fault on the basis of the detachment-limited stream power model, in particular, to understand the tectonic activities in the Puqu Fault region from a series of river profiles that were extracted from the ASTER DEM.

2. Study Area

The Puqu Fault region is located in the KJFZ in Southeastern Tibet. This region is situated on the boundary of China, India and Myanmar (Figure 1). Due to the topography and remoteness, this area has been so far seldom investigated.

2.1. The Karakoram–Jiali Fault Zone in Southeastern Tibet

Southeastern Tibet is an area very limitedly studied especially for tectonic evolution, despite that its importance has already been indicated by several studies. Booth *et al.* [32] claimed that an important element of understanding the tectonics of Southeastern Asia is by tracing the assembly of Tibet itself. To a larger extent, some studies indicated that Tibet is generally composed of terraces accreted successively to the southern boundary of Eurasia (e.g., [33–35]). Significant features of tectonics can be readily observed in Southeastern Tibet. These observations generally suggested a complicated series of tectono-magmatic events shaping this region though more studies are fundamentally needed to further clarify these tectonic activities.

As indicated in Figure 2, a mixture of normal and strike-slip faulting may summarize those active tectonics in Southern Tibet [34,36,37]. The normal faults are oriented in the direction of North-South and accordingly may reflect an East-West extrusion. Those North-South faults are widespread despite that the active Indian Plate is moving northward with reference to the relatively dormant Eurasia Plate at a rate about 4 cm/year [38]. A typical strike-slip system in Tibet is located in the KJFZ. It is

composed of a group of Northwest-Southeast aligned, right-lateral faults which appear to form the normal fault system in Southern Tibet [36]. In the East, the KJFZ is primarily bounded by the Jiali Fault Zone. The movement of the Jiali Fault is tightly associated with the clockwise rotation and the extruded body of Eastern Tibet, and is closely connected with the northeastward indentation of the India Plate, and such activity results from the indentation of the India Plate into the Eurasia Plate as well as the related erosion in the Eastern Himalaya Syntax [39].

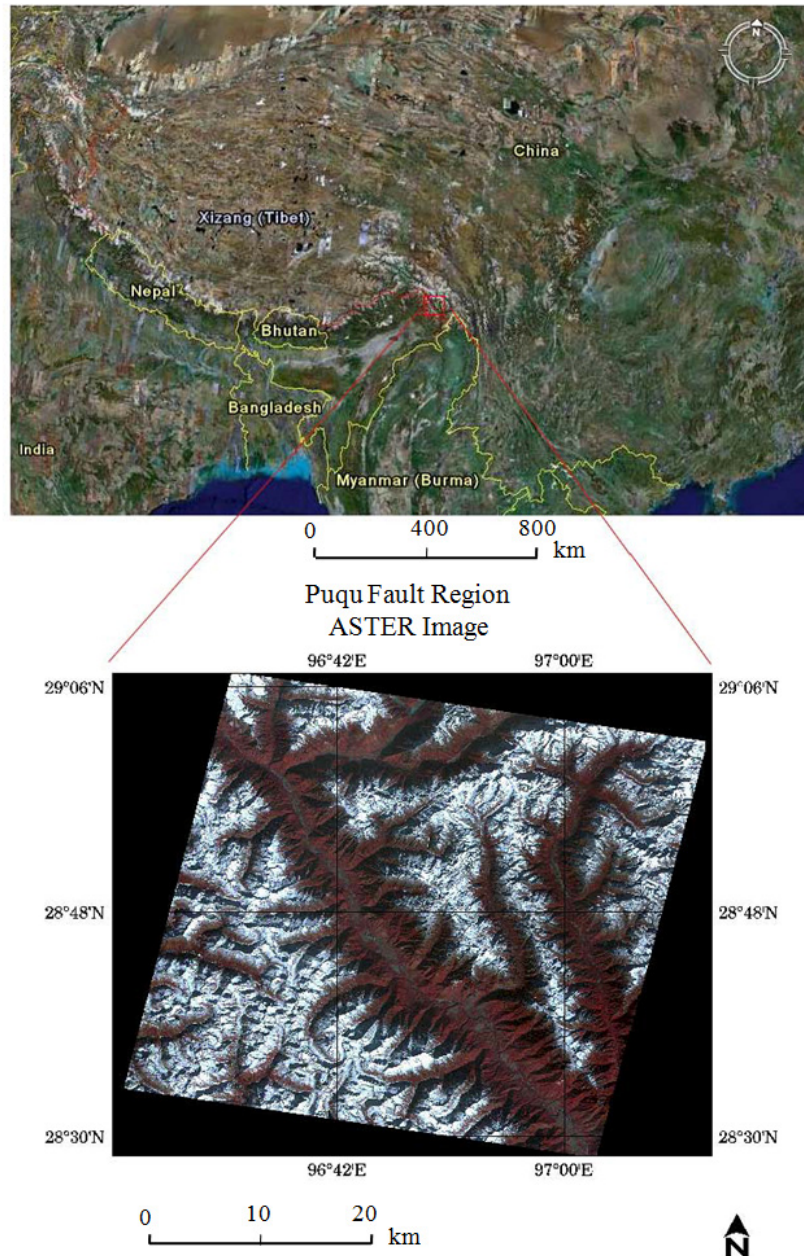


Figure 1. Location of the Puqu Fault Region. The red box shown in the upper map (information available in Google Earth) shows that the study area is located on the boundary of China, India and Myanmar. The lower map is from the ASTER image with the 3-2-1 (red-green-blue) color combination, showing the main coverage of the Puqu Fault and its surrounding area. The ASTER Level 1A data (raw digital numbers quantized as 8-bit unsigned integers) was acquired and the date of image acquisition was 3 January 2005.

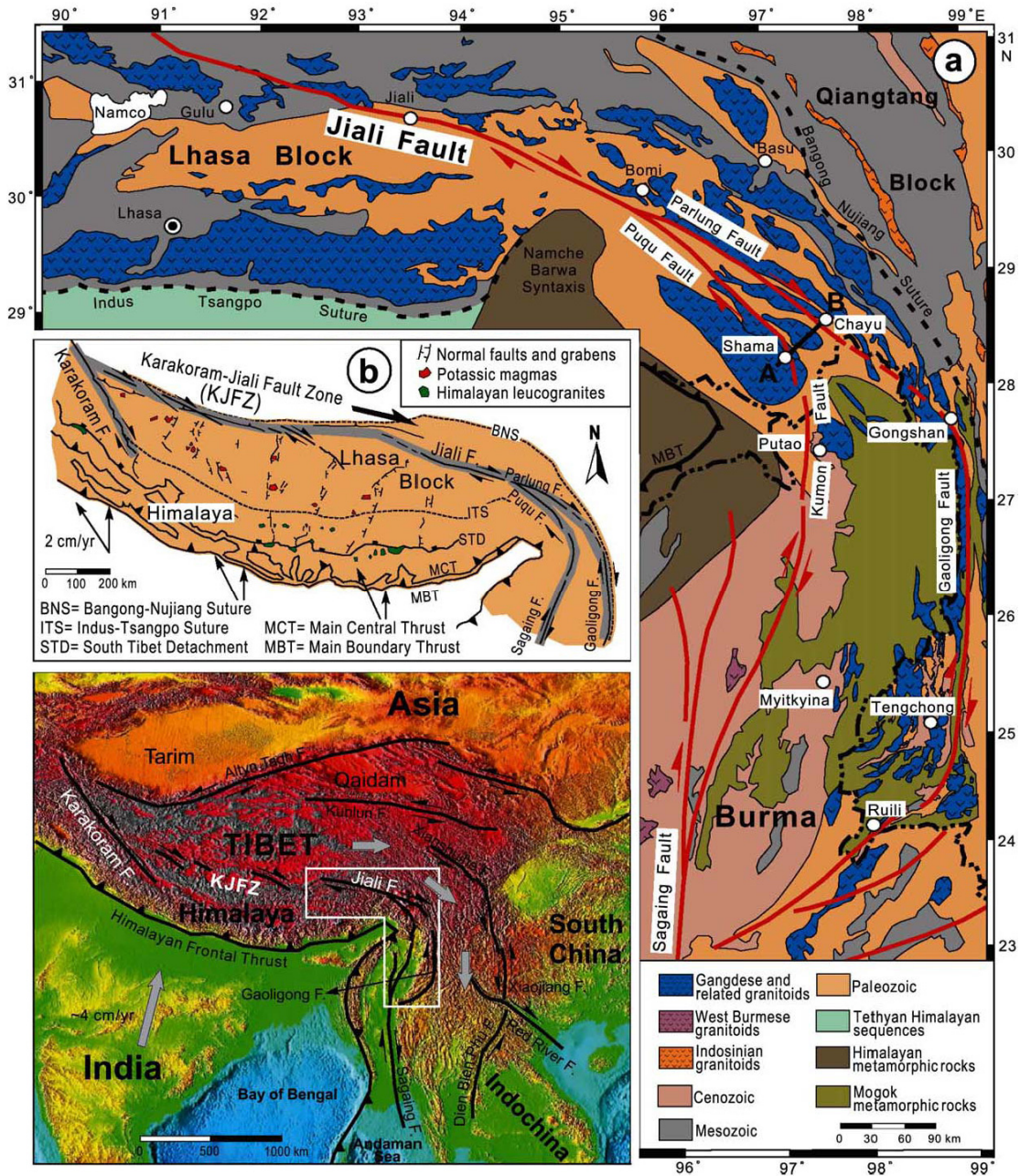


Figure 2. The topography and the principal active faults in Tibet and its adjacent regions. Here white arrows indicate the current movements of India and Northern Tibet and the ongoing clockwise rotation followed by the southward extrusion. (a) The simplified geologic map of the study area; (b) The tectonic map showing the activities of the Himalayas and Southern Tibet. Reprint with the permission of [36], 2003 copyright Elsevier).

2.2. The Puqu Fault Region

Figure 3 indicates the drainage pattern of the Puqu Fault region. In the North of the Eastern Himalayan Syntaxis, the Jiali Fault extends to Southeast and separates into two main easternmost branches, namely the Puqu Fault in the South and the Parlung Fault in the North, which extends southeastward to the Gaoligong Fault [40]. This study mainly focuses on the southern branch, the Puqu Fault. As an area of the easternmost Jiali Fault, the Puqu Fault is located in a principal active fault zone and is

influenced by the eastward extrusion of Northern Tibet as well as the clockwise rotation followed by the southward extrusion.

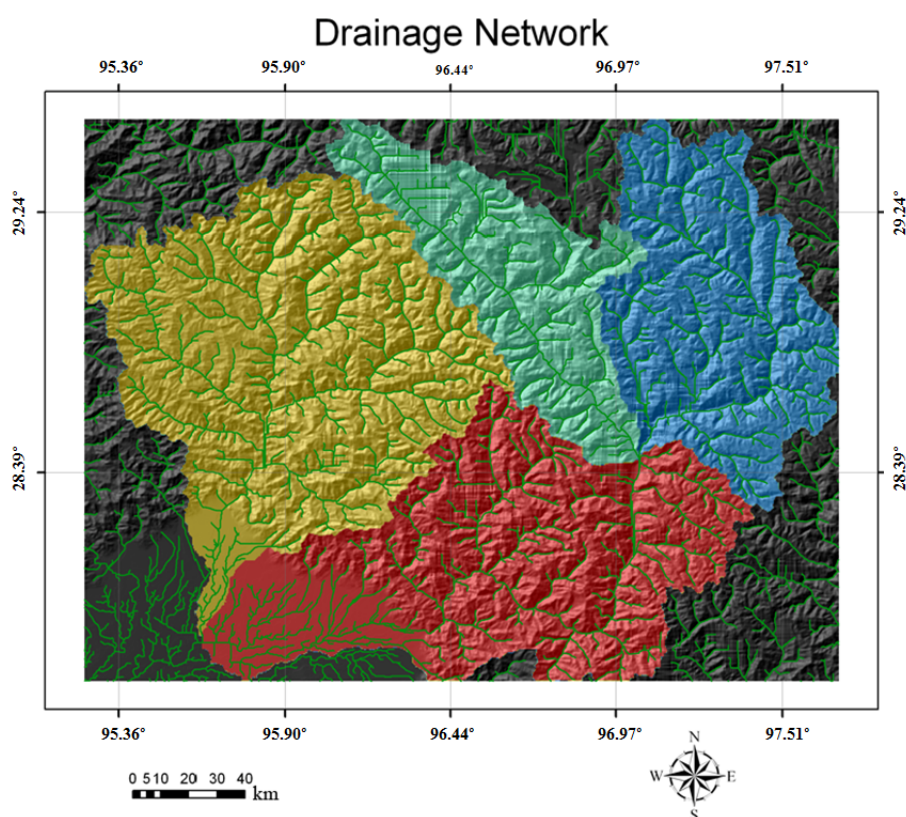


Figure 3. The drainage system in the Puqu Fault Region. Different colors indicate diverse subbasins extracted.

Literature is very limited about the tectonic evolution in the Puqu Fault region. Chung *et al.* [39] concluded that during 23–19 Ma, the northern branch of the Jiali Fault, the Parlung Fault (Figure 2), had undergone intensive strike-slip activities. In addition, Chung *et al.* [39] argued that an uplift that occurred during 10–6 Ma was related to an event which happened in the region of Himalaya as well as Eastern Tibet. The uplifting is then considered to be a regional event that may result from the indentation of the India Plate into the Eurasia Plate. In a more detailed study conducted by Lee *et al.* [36], rock samples from the Puqu Fault were collected via a Northeast-Southwest transverse, along which a large amount of sheared granitoids was discovered. Lee *et al.* [36] showed that these rocks always contain garnet or sillimanite, and corresponding peak metamorphic temperatures and pressures are considered to be higher than 550 °C and around 3–5 kbar. The triangle-shaped Indochina continent is featured by the Cenozoic convergence between the Indian and Asian Plates that developed the Indian-Asian continental collision [41–43].

So far, the Puqu Fault region has been narrowly studied due to the extreme inconvenience of field work, for instance, difficult to perform dating technology such as fission track in this remote area. As a result, the remote sensing is one important approach to investigate this area. In this study, the ASTER image was utilized to extract the tectonic indicators in the Puqu Fault region, particularly by analyzing river profiles extracted from the derived DEM that was generated from a stereo pair of images.

3. Methodology and Results

3.1. DEM Generation

The 30 m ASTER Global Digital Elevation Model (GDEM) is freely available, however in the Puqu Fault region its quality is not good due to some unfilled depressions. In this study the ASTER image was utilized to generate DEM, considering its low cost with decent spatial resolution (15 m). In addition, ASTER offers a back-looking stereo visible and near-infrared (VNIR) telescope with 15 m resolution in Band 3. This viewing geometry enables to generate a DEM with horizontal spatial resolution of 15 m. A DEM was created from a stereo pair of ASTER images acquired on 3 January 2005. Using the image correlation, it is possible to match pixels in these two images and then use the sensor geometry from the computed model to derive x , y , and z positions. The original ASTER images are Level-1A data products which are formally defined as reconstructed, unprocessed instrument data at full resolution. The scene center of the data is $28^{\circ}47'47''$ N and $96^{\circ}48'11''$ E with the sun elevation angle of 35° and the sun azimuth angle of 158° .

One hundred and eighty-seven pairs of tie points distributed throughout the whole image were identified in order to create an epipolar image pair of the channel 3N and 3B. The total Root Mean Square Error (RMSE) in x direction is 0.53 pixel whereas that in y direction is 0.19 pixel. The result is acceptable considering the difficulty in collecting tie points in this steep mountainous area of the Puqu Fault region. With the input of the ASTER orbital information in the software of PCI Geomatica 10, the epipolar images of a stereo pair of 3N and 3B were extracted. After obtaining the epipolar images, the DEM was extracted from the overlap extended between the epipolar image pairs. The final step was to geocode the epipolar DEM and the output was a DEM reprojected to the ground coordinate system. In this study, a DEM with a sampling interval of 20 m was generated. The final derived DEM is shown in Figure 4. Furthermore, on the basis of the derived DEM, the shaded relief map (Figure 5) was displayed in order to get a preliminary geomorphologic understanding in the Puqu Fault region.

3.2. River Network Extraction

The streamlines and river network were extracted from the generated DEM for further calculation of channel parameters. Streamlines define the flowing direction at each point on the topographic surface, starting on drainage divides, tracing the downhill water flowing path, and crossing contour lines. In terms of streamlines tracing, the D8 algorithm [44] was used to approximate the flow directions on the topographic surface and to track the flowing way from each pixel to its eight neighboring pixels. The direction from each pixel to its eight neighboring pixels was defined on the basis of steepest descent. This D8 algorithm is suitable for identifying individual channels, river networks and basin boundaries based on two assumptions: (1) the use of eight discrete flow angles; and (2) each pixel has a single flow direction. To simply put, these two assumptions restrict single stream direction into downstream neighboring pixel.

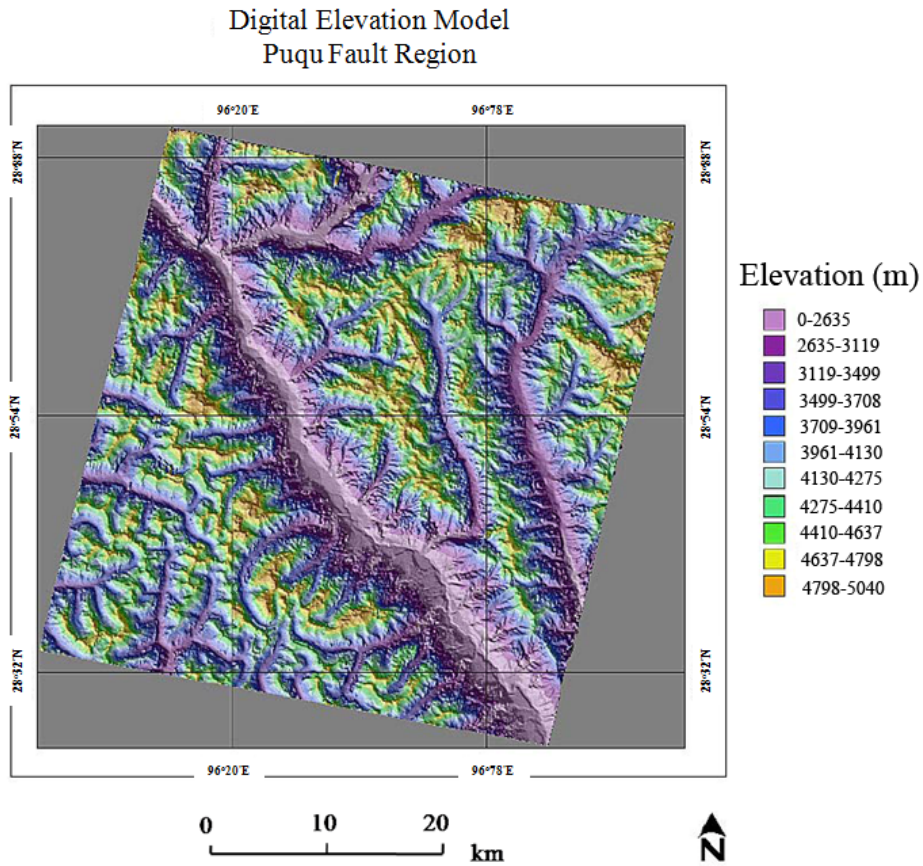


Figure 4. The digital elevation model (DEM) derived from the ASTER stereo pair images for the Puqu Fault region.

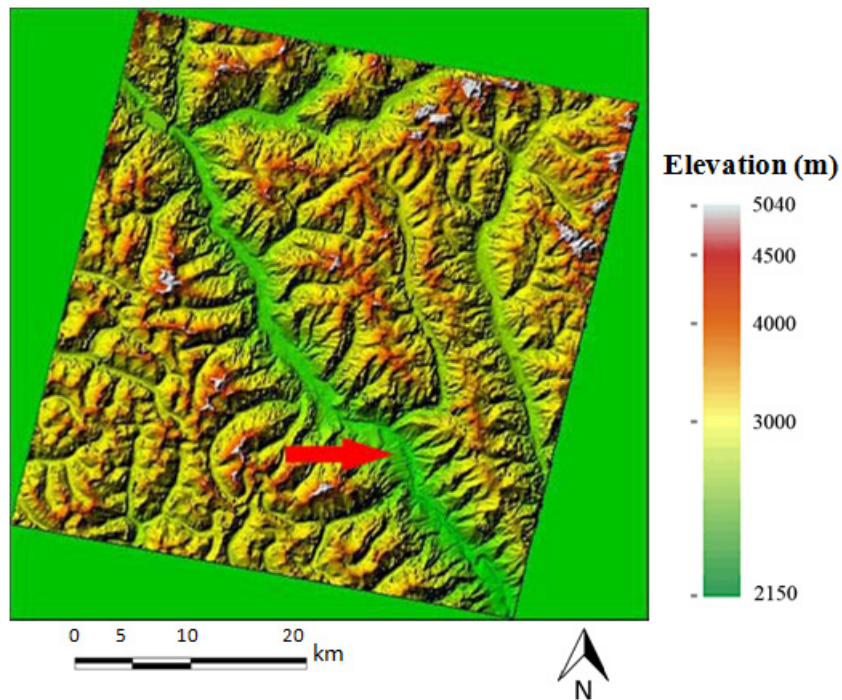


Figure 5. The shaded relief map of the Puqu Fault region with the simulated sun compass angle of 135° and the zenith angle of 40° . The red arrow indicates the bend of the Puqu Fault.

In order to establish a D8 flow grid, the imposed gradients method was utilized to resolve the flow direction in flats that contain pixels not having a neighboring pixel with lower elevation. This method mainly focuses on centering flows within flat valleys and reducing parallel flows. Moreover, the D8 flow grid was created from raster into vector. All pixels that have a flow code of zero were treated as basin outlets, including four edges of the DEM and pixels containing no data within the DEM. The derived vector file stores data for a single basin or several disjoint subbasins. Every pixel in a particular basin is the outlet pixel for a subbasin that is contained in it. Each of these subbasins records several attributes, such as contributing area and relief. This vector file stores all of these attributes for all of the pixels/subbasins.

Furthermore, two vector files were created in the software River Tools 3.0. One was the link file that stores attributes for every channel link in the river network, and the other was a stream file that records attributes for every Horton–Strahler stream in the river network. The Strahler Stream Order was employed to define the threshold when extracting the river network. In this study, the Strahler Order of the main river along the Puqu Fault was set to 5. The extraction threshold was defined as the Strahler Order ≥ 3 . The derived river network is shown in Figure 6. However, when subsequently calculating the concavity and steepness index of the extracted streams, channels with Strahler Order ≥ 4 were selected to extract the main stem and its tributaries.

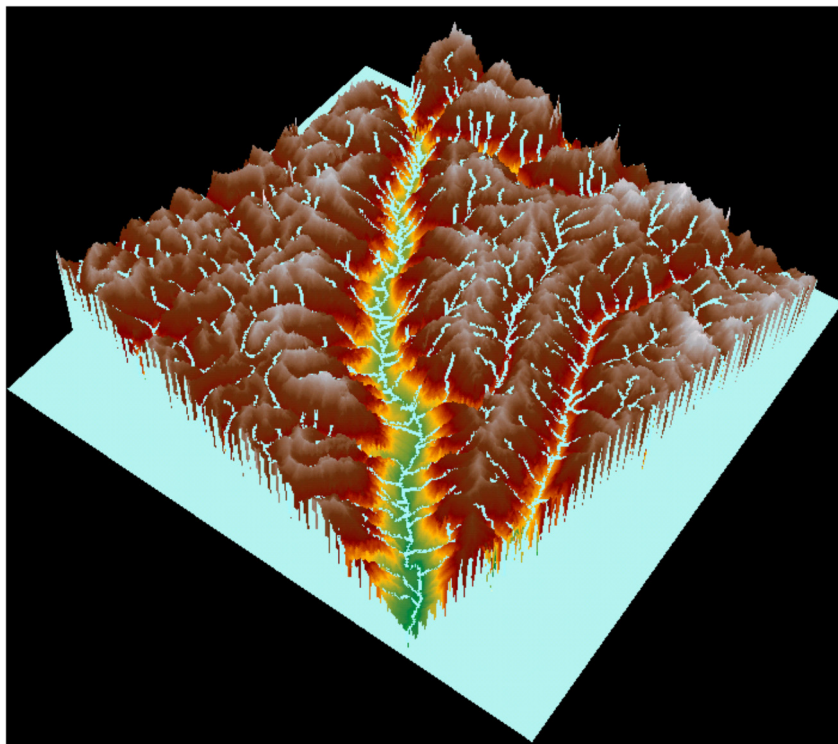


Figure 6. The channels were vectorized and exported in 3D view with DEM. The streams with Strahler Order < 3 were excluded. The elevation range is from 2150 to 5040 m. The approximate size of the domain is about 1400 km².

Finally, all streams with the Strahler Stream Order ≥ 4 were exported into dBASE Table files (.dbf). The dBASE Table files were then imported into EXCEL and MATLAB for further river profile analysis.

3.3. River Profile Analysis

River incision is often modeled as competition between uplift and erosion activities with change rates of channel elevation [19,21,45]. In the model, river profile evolution is simulated as an equation:

$$\frac{dz}{dt} = U(x,t) - E(x,t) \quad (2)$$

dz/dt represents the temporal rate of changes of channel elevation, U indicates the rock uplift rate with respect to a fixed base level and E refers to erosion rate. The erosion process can be described as an empirical relation with the expression:

$$E = KA^m S^n \quad (3)$$

S and A represent the local channel gradient and the upstream drainage area, respectively. K is identified as a dimensional coefficient of erosion whereas m and n are positive constants related to basin hydrology, erosion process and hydraulic geometry [19,21,31,45,46]. Combining Equation (2) with Equation (3), the incision model can be derived as:

$$\frac{dz}{dt} = U(x,t) - KA^m S^n \quad (4)$$

In the cases of steady-state ($dz/dt = 0$), with uniform U and K as well as constants m and n , Equation (4) can be further expressed as the equilibrium channel gradient:

$$S_e = (U / K)^{1/n} A^{-(m/n)} \quad (5)$$

Equation (5) describes the relationship between channel gradient and drainage area. It is often simplified as a power-law function as $S = k_s A^{-\theta}$ previously mentioned in Equation (1) with the coefficient k_s representing the channel steepness, equivalent to (when combining Equations (1) and (5)):

$$k_s = (U / K)^{1/n} \quad (6)$$

Equation (6) is often recognized as a strong empirical support for a positive correlation between the steepness index k_s and the rock uplift rate U (e.g., [19,21]). The coefficient θ , which represents the intrinsic channel concavity, replaces the ratio m/n , written as:

$$\theta = m / n \quad (7)$$

Equation (7) shows that channel concavity θ is related to the constants m and n . What is more important, as for m and n , it is very difficult to obtain them from natural field experiments. Channel concavity θ , namely, the ratio of m/n , is easier to be estimated [31,47]. Although the concavity value is theoretically expected to range from 0.35 to 0.6, the observed concavity may be higher considering non-uniform uplift, non-uniform lithology or variations in sediment flux and grain size [4,31].

After extracting the river network in the Puqu Fault region, the next step is to derive the channel parameters such as concavity and steepness from stream elevation profiles. In this study the concavity and steepness were calculated directly from regressions on logarithm slope-area plot. Based on Equation (1), when taking logarithm on both sides of the equation, the equation can be written as:

$$\log S = \log k_s + \log A^{-\theta} \quad (8)$$

and after reforming the Equation (8), the equation turns into:

$$\log S = -\theta \log A + \log k_s \tag{9}$$

Equation (9) indicates that it can get the information of concavity and steepness by putting slope S and drainage area A in the log-log plot and then drawing the linear regression fit line.

Using the generated 20 m resolution ASTER DEM, stream elevation profiles were extracted for 54 tributaries to the Puqu Fault in Southeastern Tibet, with the defined Strahler Order ≥ 4 . Among them, six streams were eliminated because of large pitfalls due to the quality of DEM which cannot be filled. By analyzing the elevation profile and the area-slope plot of each stream, it shows that the channels can be generally defined as two morphologic types (Figure 7). The first one is shown in Figure 7a. It represents the stream containing only one lower concave segment in the river profile and the upper segment is absent or hardly recognized. The downwards linear fit can be identified in the area-slope plot. The second type, as shown in Figure 7b, indicates the stream consisting of two concave channel segments. The upper segment and lower segment are separated by convex transition zones, namely knickzones. The corresponding two downwards fits can be found in area-slope plot separated by data with upwards trend. The channel concavity and steepness were calculated for each upper segment with minimum length of 15 pixels (300 m) and each lower segment with minimum length of 25 pixels (500 m) based on the regression fit. The Root Mean Square Error (RMSE) of each regression was calculated and regressions with RMSE greater than 0.1 were not taken into consideration. The overall regression result for all streams is shown in Table 1. The corresponding location of the streams can be found in Figure 8. The streams 13, 29, 30, 32, 46 and 52 which contain depression areas were eliminated, marked as N/A. Among the remaining 48 rivers, 32 of them were detected with both upper and lower concave segments. The remaining 16 streams were only found with the lower concave segment. The channel parameters of convex segments were not calculated because they may indicate transiting knickzones and have not formed the new equilibrium response yet. Alternatively, convexities of river profiles may be interpreted as a transient response of the river system to the change in tectonic uplift.

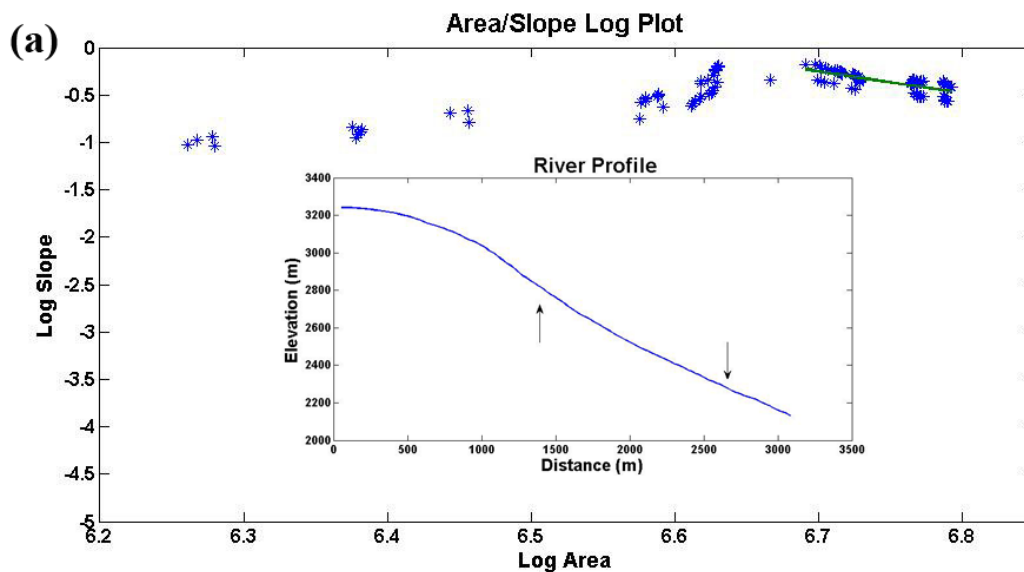


Figure 7. Cont.

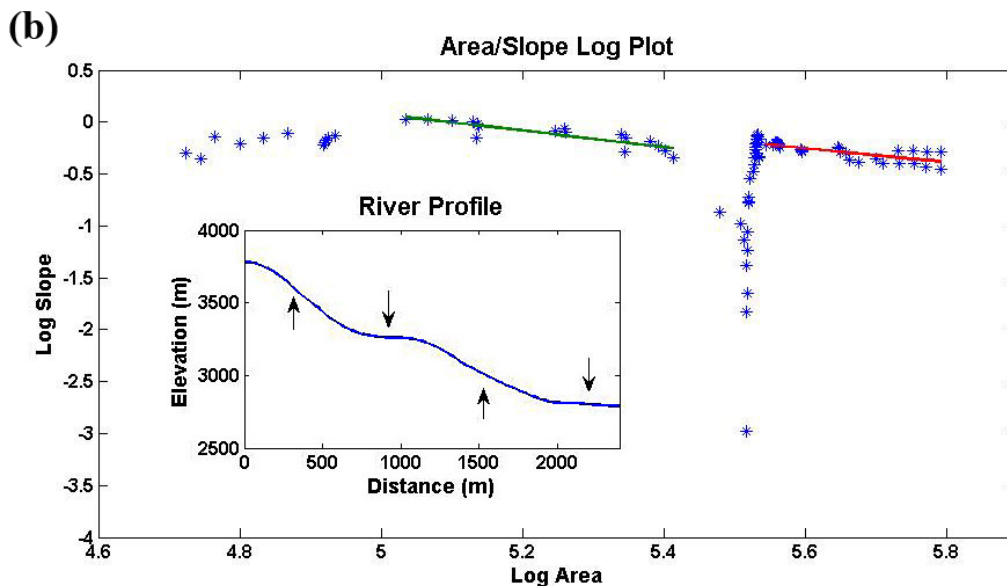


Figure 7. River elevation profiles and slope-area plots extracted from a 20 m ASTER DEM for two representative tributary types. (a) The example of a stream with one concave channel segment; (b) The example of a stream with two concave channel segments, one in the upper segment and another in the lower segment. The lines represent the linear regression fit. The arrows indicate the range of each concave segment.

Table 1. Streams: Regression Fits, RMSE, Concavity (θ) and Logarithm Steepness ($\log k_s$).

Stream	Lower Segment		Upper Segment		Lower Segment		Upper Segment	
	Regression Fit	RMSE	Regression Fit	RMSE	θ	$\log k_s$	θ	$\log k_s$
1	$y = 8.13 - 1.26x$	0.058	$y = 1.58 - 0.33x$	0.069	1.26	8.13	0.33	1.58
2	$y = 8.46 - 1.38x$	0.042	$y = 1.65 - 0.37x$	0.056	1.38	8.46	0.37	1.65
3	$y = 9.30 - 1.60x$	0.060	$y = 0.38 - 0.14x$	0.047	1.60	9.30	0.14	0.38
4	$y = 3.19 - 0.61x$	0.047	$y = 0.91 - 0.20x$	0.092	0.61	3.19	0.20	0.91
5	$y = 15.06 - 2.28x$	0.068	-	-	2.28	15.06	-	-
6	$y = 5.89 - 0.99x$	0.074	$y = 2.69 - 0.44x$	0.059	0.99	5.89	0.44	2.69
7	$y = 10.80 - 1.60x$	0.094	$y = 2.83 - 0.52x$	0.087	1.60	10.80	0.52	2.83
8	$y = 12.33 - 2.00x$	0.054	-	-	2.00	12.33	-	-
9	$y = 7.20 - 1.11x$	0.055	-	-	1.11	7.20	-	-
10	$y = 3.11 - 0.66x$	0.066	-	-	0.66	3.11	-	-
11	$y = 21.35 - 2.86x$	0.078	$y = 19.27 - 2.70x$	0.063	2.86	21.35	2.70	19.27
12	$y = 7.30 - 1.35x$	0.066	-	-	1.35	7.30	-	-
13*	N/A	-	N/A	-	N/A	-	N/A	-
14	$y = 8.99 - 1.48x$	0.068	-	-	1.48	8.99	-	-
15	$y = 5.60 - 0.87x$	0.074	-	-	0.87	5.60	-	-
16	$y = 13.61 - 2.18x$	0.054	$y = 7.27 - 1.24x$	0.057	2.18	13.61	1.24	7.27
17	$y = 9.62 - 1.46x$	0.082	$y = 4.67 - 0.97x$	0.069	1.46	9.62	0.97	4.67
18	$y = 21.31 - 3.29x$	0.065	$y = 9.19 - 1.45x$	0.076	3.29	21.31	1.45	9.19
19	$y = 42.05 - 6.67x$	0.063	-	-	6.67	42.05	-	-
20	$y = 59.87 - 8.48x$	0.084	$y = 23.34 - 3.38x$	0.075	8.48	59.87	3.38	23.34

Table 1. Cont.

Stream	Lower Segment		Upper Segment		Lower Segment		Upper Segment	
	Regression Fit	RMSE	Regression Fit	RMSE	θ	$\log k_s$	θ	$\log k_s$
21	$y = 35.20 - 5.45x$	0.070	$y = 8.00 - 1.34x$	0.087	5.45	35.20	1.34	8.00
22	$y = 54.60 - 7.42x$	0.086	-	-	7.42	54.60	-	-
23	$y = 65.95 - 10.12x$	0.086	$y = 46.87 - 7.13x$	0.066	10.12	65.95	7.13	46.87
24	$y = 46.20 - 7.15x$	0.068	$y = 20.73 - 3.24x$	0.081	7.15	46.20	3.24	20.73
25	$y = 55.67 - 7.50x$	0.093	$y = 12.22 - 1.76x$	0.080	7.50	55.67	1.76	12.22
26	$y = 35.92 - 5.38x$	0.089	$y = 10.02 - 1.92x$	0.075	5.38	35.92	1.92	10.02
27	$y = 29.86 - 4.44x$	0.060	$y = 7.49 - 1.16x$	0.069	4.44	29.86	1.16	7.49
28	$y = 20.62 - 3.00x$	0.075	$y = 15.65 - 2.31x$	0.057	3.00	20.62	2.31	15.65
29*	N/A	-	N/A	-	N/A	-	N/A	-
30*	N/A	-	N/A	-	N/A	-	N/A	-
31	$y = 19.36 - 2.81x$	0.068	-	-	2.81	19.36	-	-
32*	N/A	-	N/A	-	N/A	-	N/A	-
33	$y = 21.42 - 3.14x$	0.059	$y = 0.55 - 0.16x$	0.065	3.14	21.42	0.16	0.55
34	$y = 20.19 - 3.34x$	0.089	$y = 10.02 - 1.92x$	0.075	3.34	20.19	1.92	10.02
35	$y = 10.93 - 1.63x$	0.069	$y = 4.72 - 0.75x$	0.060	1.63	10.93	0.75	4.72
36	$y = 4.34 - 0.74x$	0.091	$y = 0.66 - 0.14x$	0.082	0.74	4.34	0.14	0.66
37	$y = 8.37 - 1.38x$	0.071	$y = 0.10 - 0.05x$	0.074	1.38	8.37	0.05	0.10
38	$y = 9.30 - 1.45x$	0.057	$y = 3.77 - 0.67x$	0.076	1.45	9.30	0.67	3.77
39	$y = 21.25 - 3.29x$	0.081	$y = 4.84 - 0.84x$	0.079	3.29	21.25	0.84	4.84
40	$y = 27.44 - 3.92x$	0.091	$y = 3.37 - 0.57x$	0.012	3.92	27.44	0.57	3.37
41	$y = 33.15 - 4.89x$	0.073	$y = 21.59 - 3.25x$	0.071	4.89	33.15	3.25	21.59
42	$y = 17.15 - 2.99x$	0.068	-	-	2.99	17.15	-	-
43	$y = 6.10 - 1.05x$	0.066	$y = 0.63 - 0.14x$	0.076	1.05	6.10	0.14	0.63
44	$y = 12.09 - 1.74x$	0.061	$y = 11.35 - 1.74x$	0.075	1.74	12.09	1.74	11.35
45	$y = 6.10 - 1.03x$	0.072	-	-	1.03	6.10	-	-
46*	N/A	-	N/A	-	N/A	-	N/A	-
47	$y = 31.84 - 5.13x$	0.076	$y = 1.88 - 0.35x$	0.070	5.13	31.84	0.35	1.88
48	$y = 43.41 - 6.60x$	0.083	-	-	6.60	43.41	-	-
49	$y = 54.32 - 7.52x$	0.072	-	-	7.52	54.32	-	-
50	$y = 71.67 - 10.21x$	0.082	$y = 21.98 - 3.25x$	0.067	10.21	71.67	3.25	21.98
51	$y = 29.29 - 4.17x$	0.081	-	-	4.17	29.29	-	-
52*	N/A	-	N/A	-	N/A	-	N/A	-
53	$y = 24.61 - 3.55x$	0.077	$y = 28.94 - 4.17x$	0.076	3.55	24.61	4.17	28.94
54	$y = 40.46 - 6.19x$	0.071	-	-	6.19	40.46	-	-

Note: * The streams 13, 29, 30, 32, 46 and 52 contain depressions and are marked as N/A.

For each linear regression fitting line, based on the Equation (9), the slope of the regression fit is $-\theta$ whereas the intercept of y axis is $\log k_s$. The results of concavity and steepness are shown in Table 1.

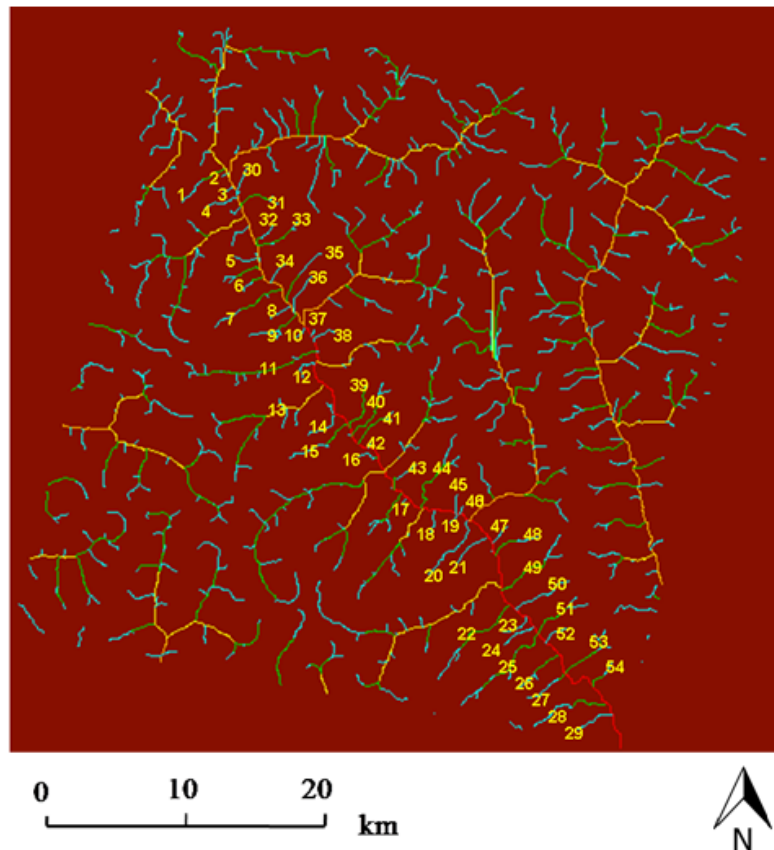


Figure 8. Location of the streams marked with the numbers from 1 to 54.

4. Discussion

4.1. Channel Equilibrium Hypothesis

The concavity and the steepness were calculated based on the stream power law (Equation (1)). In spite of the strong empirical support, the stream power-law incision model, as well as the interpretation of model parameters k_s and θ in Equations (6) and (7), is on the basis of the equilibrium channel hypothesis. Hence, the state of activity of analyzed streams can be evaluated and the usefulness of utilizing the stream power-law function in the Puqu Fault region can be anticipated. First, the uplift rates in the Tibet Plateau have been reported constantly over a long period of time. Although Spicer *et al.* [48] argued that the elevation of the Southern Tibet Plateau has remained unchanged since 15 Ma ago, other studies reported a rapid but steady uplift in the Tibet Plateau from the late Tertiary and Quaternary (e.g., [49,50]). Even for the southern Tibet fault system, no modern activity was detected [51]. Such timescale as the later Tertiary and Quaternary, is long enough in comparison with the landscape response time, and this sufficiency makes the hypothesis of steady condition plausible [52]. Secondly, the equilibrium process is continuously self-adjusting to accord with the migration of knickzones. In consequence, the new condition is always being created for the maintenance of steady state, thus forming a new equilibrium slope as the response. Because this elaboration may not be sufficient to ensure the feasibility of stream power-law function, in order to maximally avoid the misuse of the stream power-law model, all convex parts of the stream profiles were excluded, considering that under certain circumstances the large scale convexity is always related to the transition knickzone. Limited

focus on those concave profiles may maximally eliminate the possibility of transient state. Thirdly, although for some stream profiles knickzones may exist, the overall profiles of the Puqu Fault are relatively smooth and without abrupt knickpoints which are always recognized as the obvious indications of transient state. That is, the knickzone separates two equilibrated profiles: upper segments adjusted to initial conditions and lower segments adjusted to new conditions. This is in accordance with the theory that fully-attained equilibrium stream is always without major knickpoints because they generally appear with changes of uplift rate or erosion rate, and knickpoints can also result from non-uniform uplift or changes in lithology. Fourthly, despite the assumption of existing steady state, it is not plausible to assume that the model parameters can only be derived by analyzing equilibrium state data. The reason is that some data may contain both steady and transient information. And for high resolution data, by analyzing elevation profile and area-slope log plot, it is possible to differentiate the steady and transient states by analyzing knickpoints and knickzones. Sometimes it is even more important to analyze such data because it provides the possibility to detect two steady-state profiles [1]. Based on the above four reasons, to conclude, in this study it is practical to utilize the power-law stream incision model as indicated in Equation (1).

4.2. Potential Effects of Glaciations

Hobley *et al.* [53] indicated that in Indian Himalaya, glacial modification of the upper reaches of a catchment may have strong influence on the hydraulic scaling of the channel downstream, which may significantly increase the channel concavity indices of downstream reaches exceeding the expected value range of 0.3–0.6. Whether the Puqu Fault is under influence of large glaciations as appeared in other high relief places in Tibet remains an important research consideration. To attempt to understand this question, the glacier map from the Chinese Glacier Information System (CGIS) established in the year 2004 [54] was acquired. The glacier distribution in the Puqu Fault region is shown in Figure 9. As the inventory map indicates, the glaciers existing along the Puqu Fault are not as much as those in the north in the area of the Parlung Fault and these glaciers are distributed in the higher elevation area, namely the upper segment part. Although the existence of glaciers is supposed to smooth the valley and to erode the valley walls—They can also reduce relief and form plateaus if they are ice caps rather than valley glaciers—Only relatively higher concavity and steepness were observed for the stream 11. The derived concavity value is 2.70, a bit lower than the lower segment value 2.86 and much higher than the average concavity value (0.84) of those upper streams in the north of the bend. The calculated $\log k_s$ value for the upper segment is 19.27, also slightly lower than the lower segment value (21.35) but much higher than the average value (5.75) of the north bend area. Other than the stream 11, no significantly higher concavity and steepness values was noticed for those streams affected by glaciations in the upper concave segment. Thus, it may be argued that the influence of glaciations is simply limited along the Puqu Fault. Furthermore, it could be argued that the effects of past climate changes may facilitate the mountain uplift, thus resulting in the high concavity and steepness indices in the Puqu Fault region because of the post-glacial rebound effect related to the retreat of existed glaciers. However, although the theory of the post-glacial rebound is proven to be true and was verified by some studies in Europe and North America several decades ago (e.g., [55,56]), such argument in the Tibet Plateau remains to be further investigated. Although some studies proposed the hypothesis of

“ice sheet” suggesting that the former ice sheet may result in the glacial uplift in the Tibet Plateau [57], it is contradictory to the new findings that the Tibet Plateau is a young plateau rather than an ice covered plateau [58]. Also, such hypothesis has been denied by the zero-order test of the purely atmospheric response to Tibetan ice sheet forcing [59]. Even without isostatic rebound, the ice sheet may have created the low relief topography which can be depleted by incision, thus potentially causing the two segments: the top segment with low concavity and slope on the relict plateau and the lower segment with high concavity and slope in the incised part of the landscape. Therefore, it may be argued that the uplift in the Puqu Fault region is not due to the rise of land masses which were previously depressed by the huge weight of ice sheets during the past time. That is, the high concavity and steepness values of the land in Southeastern Tibet are not likely to be the consequence of post-glacial rebound. Therefore, river morphologies and profiles tend to be excluded from the significant influence of the potential glaciations.

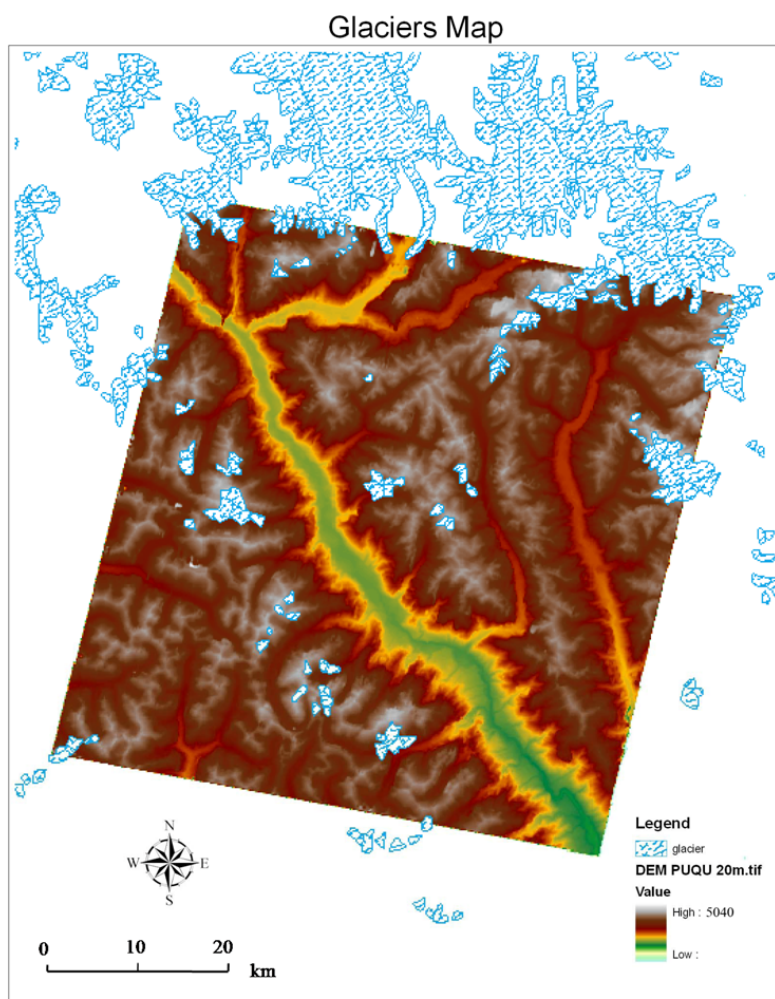


Figure 9. Distribution of glaciers in the Puqu Fault region as shown in the glacier map acquired from the Chinese Glacier Information System (CGIS).

4.3. Open Questions

In the Puqu Fault region, the topography of rivers is usually very steep. As documented above, most of the channel data have slopes in excess of 0.1 and commonly in excess of 0.3. The transition from

fluvial channels to steep debris-flow channels is usually reported at slopes between 0.1 and 0.3 [1]. In consequence, it may be argued that fluvial processes are not responsible for the observed shape of the profiles. In addition, the analysis in this study was performed on relatively short segments, though the potential use of the stream power law $S = k_s A^{-\theta}$ is usually performed on segments over a range of drainage areas. Some studies use a reference concavity index to calculate a normalized steepness index at every point along their river profiles (e.g., [25,60,61]). Although normalized steepness is useful for short channel segments, concavity is more meaningful to characterize the region where uplift rate may have systematic change along the profile.

5. Conclusions

The Puqu Fault is located in a tectonically dynamic region in Southern Tibet. This study attempted to understand the tectonic activities in the Puqu Fault region from a series of river profiles that were extracted from an ASTER DEM. The main work was composed of four parts: (1) DEM generation from two ASTER stereo pair images; (2) river network extraction from the ASTER DEM; (3) calculation of channel parameters; and (4) interpretation and discussion of the derived results. First, in terms of DEM generation for the Puqu Fault region, a total of 187 GCPs were manually chosen with a decent RMSE: 0.53 pixel along the x direction and 0.19 pixel along the y direction. The epipolar images were subsequently produced. The DEM was finalized with 20 m resolution after being resampled from the original 15 m resolution for the purpose of noise reduction. Secondly, the river network was extracted for the Puqu Fault region on the basis of the D8 algorithm with a pre-defined threshold of the Strahler Order ≥ 4 . Thirdly, the calculation of concavity θ and steepness k_s was based on the stream power law $S = k_s A^{-\theta}$. A series of 48 stream elevation profiles on both sides of the Puqu Fault were extracted and then the channel slope S and drainage area A of each profile were calculated. The study further put slope and drainage area in the logarithm plot and derived the concavity and steepness index through the linear regression. Among these 48 streams, 32 of them were detected with both upper and lower concave segments separated by intermediate transition zones, whereas the remaining 16 streams were detected only with the lower segments. For each segment, the channel parameters of concavity θ and logarithm steepness $\log k_s$ were calculated. This paper further discussed the river profile analysis which may be influenced by the following factors: (1) the usefulness of the stream power law; (2) the potential effects of glaciations; and (3) the steep topography and relatively short channel segments in this region. Currently the understanding of the tectonic activities in the Puqu Fault region is largely limited by the difficulty in accessing this area. In the future, a field trip in Southeastern Tibet area would be very beneficial for geological surveying and result validation across the Puqu Fault region.

Acknowledgments

This work was funded by the National Natural Science Foundation of China (No. 41201424), the 973 National Basic Research Program (No. 2013CB733203 and No. 2013CB733204) and the 863 National High-Tech R&D Program (No. 2012AA121302). The authors appreciate Richard Gloaguen and the Remote Sensing Group at TU Freiberg for their precious suggestions on the work.

Author Contributions

All authors contributed extensively to the study presented in this manuscript. Ping Lu proposed the methodology, analyzed the data and wrote the paper. Yu Shang is the corresponding author and is mainly responsible for data interpretation and wrote part of this paper.

Conflicts of Interest

The authors declare no conflict of interest.

References

1. Wobus, C.; Whipple, K.X.; Kirby, E.; Snyder, N.; Johnson, J.; Spyropolou, K.; Crosby, B.; Sheehan, D. Tectonics from topography: Procedures, promise, and pitfalls. *Geol. Soc. Am. Spec. Papers* **2006**, *398*, 55–74.
2. Gregory, K.M.; Chase, C.G. Tectonic and climatic significance of a late Eocene low-relief, high-level geomorphic surface, Colorado. *J. Geophys. Res. Solid Earth (1978–2012)* **1994**, *99*, 20141–20160.
3. Clark, M.K.; Royden, L.H. Topographic ooze: Building the eastern margin of Tibet by lower crustal flow. *Geology* **2000**, *28*, 703–706.
4. Schoenbohm, L.; Whipple, K.; Burchfiel, B.; Chen, L. Geomorphic constraints on surface uplift, exhumation, and plateau growth in the Red River region, Yunnan province, China. *Geol. Soc. Am. Bull.* **2004**, *116*, 895–909.
5. Burbank, D.W.; Leland, J.; Fielding, E.; Anderson, R.S.; Brozovic, N.; Reid, M.R.; Duncan, C. Bedrock incision, rock uplift and threshold hillslopes in the northwestern Himalayas. *Nature* **1996**, *379*, 505–510.
6. Heimsath, A.M.; Dietrich, W.E.; Nishiizumi, K.; Finkel, R.C. The soil production function and landscape equilibrium. *Nature* **1997**, *388*, 358–361.
7. Montgomery, D.R.; Brandon, M.T. Topographic controls on erosion rates in tectonically active mountain ranges. *Earth Planet Sci. Lett.* **2002**, *201*, 481–489.
8. Larue, J.-P. Effects of tectonics and lithology on long profiles of 16 rivers of the southern Central Massif border between the Aude and the Orb (France). *Geomorphology* **2008**, *93*, 343–367.
9. Larue, J.-P. Tectonic influences on the quaternary drainage evolution on the north-western margin of the French Central Massif: The creuse valley example. *Geomorphology* **2008**, *93*, 398–420.
10. Ambili, V.; Narayana, A. Tectonic effects on the longitudinal profiles of the Chaliyar river and its tributaries, Southwest India. *Geomorphology* **2014**, *217*, 37–47.
11. VanLaningham, S.; Meigs, A.; Goldfinger, C. The effects of rock uplift and rock resistance on river morphology in a subduction zone forearc, Oregon, USA. *Earth Surf. Process. Landf.* **2006**, *31*, 1257–1279.
12. Peters, G.; van Balen, R.T. Pleistocene tectonics inferred from fluvial terraces of the northern Upper Rhine Graben, Germany. *Tectonophysics* **2007**, *430*, 41–65.

13. Gloaguen, R.; Kabner, A.; Wobbe, F.; Shahzad, F.; Mahmood, A. Remote sensing analysis of crustal deformation using river networks. In Proceedings of the IEEE International Geoscience and Remote Sensing Symposium, 2008, IGARSS 2008, Boston, MA, USA, 7–11 July 2008; pp. IV-1–IV-4.
14. Shahzad, F.; Mahmood, S.A.; Gloaguen, R. Drainage network and lineament analysis: An approach for Potwar Plateau (Northern Pakistan). *J. Mt. Sci.* **2009**, *6*, 14–24.
15. Leeder, M.; Jackson, J. The interaction between normal faulting and drainage in active extensional basins, with examples from the Western United States and Central Greece. *Basin Res.* **1993**, *5*, 79–102.
16. Schumm, S.A.; Schumm, S.A.; Dumont, J.F.; Holbrook, J.M. *Active Tectonics and Alluvial Rivers*; Cambridge University Press: Cambridge, UK, 2002.
17. Hack, J.T. Stream-profile analysis and stream-gradient index. *J. Res. US Geol. Surv.* **1973**, *1*, 421–429.
18. Howard, A.D.; Kerby, G. Channel changes in badlands. *Geol. Soc. Am. Bull.* **1983**, *94*, 739–752.
19. Snyder, N.P.; Whipple, K.X.; Tucker, G.E.; Merritts, D.J. Landscape response to tectonic forcing: Digital elevation model analysis of stream profiles in the mendocino triple junction region, northern california. *Geol. Soc. Am. Bull.* **2000**, *112*, 1250–1263.
20. Lague, D.; Davy, P.; Crave, A. Estimating uplift rate and erodibility from the area-slope relationship: Examples from Brittany (France) and numerical modelling. *Phys. Chem. Earth A Solid Earth Geod.* **2000**, *25*, 543–548.
21. Kirby, E.; Whipple, K. Quantifying differential rock-uplift rates via stream profile analysis. *Geology* **2001**, *29*, 415–418.
22. Shahzad, F.; Gloaguen, R. Tecdem: A matlab based toolbox for tectonic geomorphology, part 1: Drainage network preprocessing and stream profile analysis. *Comput. Geosci.* **2011**, *37*, 250–260.
23. Anoop, A.; Prasad, S.; Basavaiah, N.; Brauer, A.; Shahzad, F.; Deenadayalan, K. Tectonic versus climate influence on landscape evolution: A case study from the upper Spiti Valley, NWHimalaya. *Geomorphology* **2012**, *145*, 32–44.
24. Fuchs, M.C.; Gloaguen, R.; Pohl, E. Tectonic and climatic forcing on the Panj river system during the Quaternary. *Int. J. Earth Sci.* **2013**, *102*, 1985–2003.
25. Kirby, E.; Whipple, K.X. Expression of active tectonics in erosional landscapes. *J. Struct. Geol.* **2012**, *44*, 54–75.
26. Mahmood, S.A.; Gloaguen, R. Appraisal of active tectonics in hindu kush: Insights from DEM derived geomorphic indices and drainage analysis. *Geosci. Front.* **2012**, *3*, 407–428.
27. Vezzoli, G.; Garzanti, E.; Vincent, S.J.; Andò, S.; Carter, A.; Resentini, A. Tracking sediment provenance and erosional evolution of the western greater caucasus. *Earth Surf. Process. Landf.* **2014**, *39*, 1101–1114.
28. Florinsky, I.; Eilers, R.G.; Manning, G.; Fuller, L. Prediction of soil properties by digital terrain modelling. *Environ. Model. Softw.* **2002**, *17*, 295–311.
29. Lindsay, J.B. The terrain analysis system: A tool for hydro-geomorphic applications. *Hydrol. Process.* **2005**, *19*, 1123–1130.
30. Foster, M.A.; Kelsey, H.M. Knickpoint and knickzone formation and propagation, South Fork Eel River, northern California. *Geosphere* **2012**, *8*, 403–416.

31. Whipple, K.X.; Tucker, G.E. Dynamics of the stream-power river incision model: Implications for height limits of mountain ranges, landscape response timescales, and research needs. *J. Geophys. Res. Solid Earth (1978–2012)* **1999**, *104*, 17661–17674.
32. Booth, A.L.; Zeitler, P.K.; Kidd, W.S.; Wooden, J.; Liu, Y.; Idleman, B.; Hren, M.; Chamberlain, C.P. U-Pb zircon constraints on the tectonic evolution of Southeastern Tibet, Namche Barwa area. *Am. J. Sci.* **2004**, *304*, 889–929.
33. Murphy, M.; Yin, A.; Harrison, T.; Dürr, S.; Chen, Z.; Ryerson, F.; Kidd, W.; Wang, X.; Zhou, X. Did the Indo-Asian collision alone create the Tibetan plateau? *Geology* **1997**, *25*, 719–722.
34. Yin, A.; Harrison, T.M. Geologic evolution of the Himalayan-Tibetan Orogen. *Ann. Rev. Earth Planet. Sci.* **2000**, *28*, 211–280.
35. Kapp, P.; Murphy, M.A.; Yin, A.; Harrison, T.M.; Ding, L.; Guo, J. Mesozoic and cenozoic tectonic evolution of the shiquanhe area of Western Tibet. *Tectonics* **2003**, *22*, doi:10.1029/2001TC001332.
36. Lee, H.-Y.; Chung, S.-L.; Wang, J.-R.; Wen, D.-J.; Lo, C.-H.; Yang, T.F.; Zhang, Y.; Xie, Y.; Lee, T.-Y.; Wu, G. Miocene Jiali Faulting and its implications for Tibetan tectonic evolution. *Earth Planet. Sci. Lett.* **2003**, *205*, 185–194.
37. Tapponnier, P.; Zhiqin, X.; Roger, F.; Meyer, B.; Arnaud, N.; Wittlinger, G.; Jingsui, Y. Oblique stepwise rise and growth of the Tibet Plateau. *Science* **2001**, *294*, 1671–1677.
38. Wang, Q.; Zhang, P.-Z.; Freymueller, J.T.; Bilham, R.; Larson, K.M.; Lai, X.a.; You, X.; Niu, Z.; Wu, J.; Li, Y. Present-day crustal deformation in china constrained by global positioning system measurements. *Science* **2001**, *294*, 574–577.
39. Chung, L.; Yang, T.; Chung, S.; Liu, T.; Walia, M.; Lo, C. Fission track ages as evidence for the thermal history of Jiali Fault (Eastern Tibet) and its tectonic implications. In Proceedings of AGU Fall Meeting, San Francisco, CA, USA, 11–15 December 2006; p. 1577.
40. Searle, M.; Elliott, J.; Phillips, R.; Chung, S.-L. Crustal-lithospheric structure and continental extrusion of tibet. *J. Geol. Soc.* **2011**, *168*, 633–672.
41. Peltzer, G.; Tapponnier, P. Formation and evolution of strike-slip faults, rifts, and basins during the India-Asia collision: An experimental approach. *J. Geophys. Res. Solid Earth (1978–2012)* **1988**, *93*, 15085–15117.
42. Replumaz, A.; Tapponnier, P. Reconstruction of the deformed collision zone between India and Asia by backward motion of lithospheric blocks. *J. Geophys. Res. Solid Earth (1978–2012)* **2003**, *108*, doi:10.1029/2001JB000661.
43. Song, S.; Niu, Y.; Wei, C.; Ji, J.; Su, L. Metamorphism, anatexis, zircon ages and tectonic evolution of the gongshan block in the northern indochina continent—An eastern extension of the lhasa block. *Lithos* **2010**, *120*, 327–346.
44. O'Callaghan, J.F.; Mark, D.M. The extraction of drainage networks from digital elevation data. *Comput. Vis. Graph. Image Process.* **1984**, *28*, 323–344.
45. Howard, A.D. A detachment-limited model of drainage basin evolution. *Water Resour. Res.* **1994**, *30*, 2261–2285.
46. Whipple, K.X.; Hancock, G.S.; Anderson, R.S. River incision into bedrock: Mechanics and relative efficacy of plucking, abrasion, and cavitation. *Geol. Soc. Am. Bull.* **2000**, *112*, 490–503.
47. Seidl, M.; Dietrich, W. The problem of channel erosion into bedrock. *Catena Suppl.* **1993**, *23*, 101–101.

48. Spicer, R.A.; Harris, N.B.; Widdowson, M.; Herman, A.B.; Guo, S.; Valdes, P.J.; Wolfe, J.A.; Kelley, S.P. Constant elevation of southern Tibet over the past 15 million years. *Nature* **2003**, *421*, 622–624.
49. Dewey, J.F.; Shackleton, R.M.; Chengfa, C.; Yiyin, S. The tectonic evolution of the Tibetan Plateau. *Philos. Trans. R. Soc. Lond. Ser. A Math. Phys. Sci.* **1988**, *327*, 379–413.
50. Harrison, T.M.; Copeland, P.; Hall, S.A.; Quade, J.; Burner, S.; Ojha, T.P.; Kidd, W. Isotopic preservation of Himalayan/Tibetan uplift, denudation, and climatic histories of two molasse deposits. *J. Geol.* **1993**, *101*, 157–175.
51. Kirby, E.; Whipple, K.X.; Tang, W.; Chen, Z. Distribution of active rock uplift along the eastern margin of the Tibetan Plateau: Inferences from bedrock channel longitudinal profiles. *J. Geophys. Res. Solid Earth (1978–2012)* **2003**, *108*, doi:10.1029/2001JB000861.
52. Whipple, K.X. Fluvial landscape response time: How plausible is steady-state denudation? *Am. J. Sci.* **2001**, *301*, 313–325.
53. Hobbey, D.E.; Sinclair, H.D.; Cowie, P.A. Processes, rates, and time scales of fluvial response in an ancient postglacial landscape of the Northwest Indian Himalaya. *Geol. Soc. Am. Bull.* **2010**, *122*, 1569–1584.
54. Wu, L.; Li, X. *China Glacier Information System*; Ocean Press: Beijing, China, 2004; p. 135. (In Chinese)
55. Farrand, W.R. Postglacial uplift in north america. *Am. J. Sci.* **1962**, *260*, 181–199.
56. Andrews, J. Postglacial rebound in arctic Canada: Similarity and prediction of uplift curves. *Can. J. Earth Sci.* **1968**, *5*, 39–47.
57. Kuhle, M. Glacial isostatic uplift of Tibet as a consequence of a former ice sheet. *Geo J.* **1995**, *37*, 431–449.
58. Harris, N. The elevation history of the Tibetan Plateau and its implications for the Asian monsoon. *Palaeogeogr. Palaeoclimatol. Palaeoecol.* **2006**, *241*, 4–15.
59. Lautenschlager, M.; Santer, B.D. Atmospheric response to a hypothetical Tibetan ice sheet. *J. Clim.* **1991**, *4*, 386–394.
60. Kirby, E.; Ouimet, W. Tectonic geomorphology along the eastern margin of Tibet: Insights into the pattern and processes of active deformation adjacent to the Sichuan basin. *Geol. Soc. Lond. Spec. Publ.* **2011**, *353*, 165–188.
61. Regalla, C.; Kirby, E.; Fisher, D.; Bierman, P. Active forearc shortening in Tohoku, Japan: Constraints on fault geometry from erosion rates and fluvial longitudinal profiles. *Geomorphology* **2013**, *195*, 84–98.